Estuarine, Coastal and Shelf Science 253 (2021) 107291

Contents lists available at ScienceDirect

Estuarine, Coastal and Shelf Science

journal homepage: http://www.elsevier.com/locate/ecss

Internal tidal waves and deep-water renewal in a tropical fjord: Lessons from Ambon Bay, eastern Indonesia

Gerry Giliant Salamena [a,b,c,*], James C. Whinney [b], Scott F. Heron [a,b], Peter V. Ridd [d]

[a] Physical Sciences, College of Science and Engineering, James Cook University, Townsville, QLD, Australia 4811
[b] Marine Geophysics Laboratory, College of Science and Engineering, James Cook University, Townsville, QLD, Australia 4811
[c] Marine Physics Division at Centre for Deep-Sea Research (CDSR) of Indonesian Institute of Sciences (LIPI), Jalan Y. Syaranamual, Kampung Guru-guru, Desa Poka, Kota Ambon, Provinsi Maluku, 97233, Indonesia
[d] 34 Mango Avenue, Mundingburra, Townsville, QLD, Australia, 4812

ARTICLE INFO

Keywords:
Deep-water renewal
Tropical fjord
Internal tides
Flushing capacity
Ambon Bay

ABSTRACT

Seasonal-varying internal tidal dynamics have a critical role in deep-water renewal in tropical shallow-silled fjords (e.g. Ambon Bay, Indonesia). Seasonal- and tidal-based longitudinal CTD casts from the slope of outer Ambon Bay (OAB) to the sill of Ambon Bay coupled with bottom-mounted current meters at the sill and in inner Ambon Bay (IAB, the fjord basin), were employed to investigate the internal tidal-sill slope interaction and the characteristics of deep-water inflow. Weaker stratification in the easterly monsoonal season than the transitional monsoonal season (dT/dz = ~0.02 °C/m *cf.* dT/dz = ~0.06 °C/m) drives the predominant sub-critical slope condition at the OAB slope causing more frequent tidal upwelling events in the easterly monsoonal season (13 events in a spring-neap sequence) than in the transitional monsoonal season (5 events). The magnitude of tidal upwelling in Ambon Bay, as measured by the depth from which water upwells, is stronger in the easterly monsoonal season (up to 200 m) than in the transitional monsoonal season (maximum: 115 m). The influx of upwelled water across the sill was controlled by the tidal excursion of the deep-water plume in the easterly monsoonal season and by the deep-water/sill density difference in the transitional monsoonal season. A series of deep-water renewal events in IAB within a spring-neap sequence (~2 weeks) in the easterly monsoonal season supplied a total inflow volume of 0.09 ± 0.02 km^3 which can replenish approximately 80% volume of the IAB deep layer. This total inflow volume was smaller in the transitional monsoonal season (0.05 ± 0.01 km^3), hence, only flushing 40% volume of the IAB deep layer. The knowledge of internal tidal waves and deep-water inflow in Ambon Bay presented here will be a key reference for future studies focused on water transport in Ambon Bay and other shallow-silled tropical fjords.

1. Introduction

Ambon Bay in Ambon Island of eastern Indonesia (Fig. 1a) is a shallow-silled fjord with significant differences from those widely found in the high latitude regions. The bay is located in the tropics with the fjord basin (inner Ambon Bay, IAB, Fig. 1a) warmer than its outer water (outer Ambon Bay, OAB, Fig. 1a) due to rapid warming in the isolated tropical basin (Nahas et al., 2005; Putri et al., 2008; Wenno and Anderson, 1984) (see Fig. 1b and c for the geography of a fjord: fjord basin, sill and outer water). This contrasts to high latitude fjords where glacial meltwater affects temperature in the fjord basin (Belzile et al., 2016; Gade and Edwards, 1980; Pickard and Stanton, 1980). Yet, deep-water renewal, well-known in the high latitudinal fjords (Allen and Simpson, 1998; Gade and Edwards, 1980), seems to also occur in IAB and flushes the deep layer of this isolated basin below the sill depth (depth: 12 m) (Anderson and Sapulete, 1982; Wenno and Anderson, 1984). Moreover, deep-water renewal is considered to be pivotal in controlling the degree of pollution build-up in IAB driven by rapid coastal development in Ambon City (i.e. coastal area indicated by red line in Ambon Island, Fig. 1a) in the last three decades (Evans et al., 1995; Kakisina et al., 2015; Pelasula, 2008; Saiya et al., 2016; Uneputty and Evans, 1997).

Deep-water renewal in shallow-silled fjords is intermittent due to the variable supply of denser water at the sill, which is controlled by tides and water stratification at the sill slope (slope α, Fig. 1c) in the form of tidal upwelling driven by internal wave dissipation (Gade and Edwards,

* Corresponding author.Physical Sciences, College of Science and Engineering, James Cook University, Townsville, QLD, Australia, 4811.
E-mail address: gerry.salamena@my.jcu.edu.au (G.G. Salamena).

https://doi.org/10.1016/j.ecss.2021.107291
Received 14 July 2020; Received in revised form 15 February 2021; Accepted 16 February 2021
Available online 3 March 2021

1980; Staalstrøm and Røed, 2016; Stigebrandt, 1976, 1979). For example, this internal tidal dissipation process is more likely to occur when the sill slope is sub-critical i.e., α is less than the ray slope of internal wave, c, and is highly controlled by water stratification (Cacchione and Wunsch, 1974; Cacchione et al., 2002). A supercritical slope ($\alpha/c > 1$) is more likely to prevent tidal upwelling as internal waves are reflected downward to the deep ocean (Cacchione and Wunsch, 1974; Cacchione et al., 2002). Hence, seasonal water stratification (thus, seasonal internal tidal upwelling) can produce seasonal variation in deep-water renewal in the fjord basin (Allen and Simpson, 1998; Petruncio et al., 1998; Staalstrøm et al., 2012). Under strong tidal flow (e.g. spring tides), internal tidal upwelling due to internal tidal dissipation is intensified (Klymak et al., 2008, 2011; Legg and Klymak, 2008). From geographic perspectives, the latitudinal difference in water stratification due to insolation (Fiedler, 2010; Sprintall and Cronin, 2009) is likely to produce geographic differences in internal tidal dissipation and deep-water renewal in shallow-silled fjords.

Studying internal tidal dissipation and deep-water renewal in Ambon Bay is important for two main reasons. Firstly, the profoundly limited studies on these topics in the tropics (i.e. preliminary studies only in Ambon Bay) (Anderson and Sapulete, 1982; Rebert and Birowo, 1989; Wenno and Anderson, 1984) compared to those in the high latitude region (Farmer and Freeland, 1983; Gade and Edwards, 1980; Inall and Gillibrand, 2010) indicate that comprehensive studies on these topics in Ambon Bay can add important insights into the existing knowledge mostly found in high latitudes. Such limited studies in the tropics are due to the rarity of tropical fjords (i.e. there are only six tropical fjords globally of which three have shallow sill (Anderson and Sapulete, 1982; Deuser, 1975)) caused by local tectonic activities creating sills during the tropical fjord genesis (Berrangé and Thorpe, 1988; Honthaas et al., 1999; Houvenaghel, 1978; Lewerissa et al., 2018). This contrasts to the wide-spread distribution of fjords in the high latitudes due to the wide-spread glacial erosion activities in these regions during the Quaternary period (Farmer and Freeland, 1983; Holtedahl, 1967; Nesje and Whillans, 1994; Pickard and Stanton, 1980; Syvitski and Shaw, 1995). Secondly, regarding the control of deep-water renewal on pollution build-ups in shallow-silled fjords (Friedrich et al., 2014; Pearson, 1980), studying internal tidal dissipation and deep-water renewal in Ambon Bay is more important than in the other two shallow-silled tropical fjords: Kao Bay of Indonesia and Darwin Bay of Galapagos Islands (Deuser, 1975). In Kao Bay, there is much lower human population density and related coastal development (Sobari, 2009). This is also true

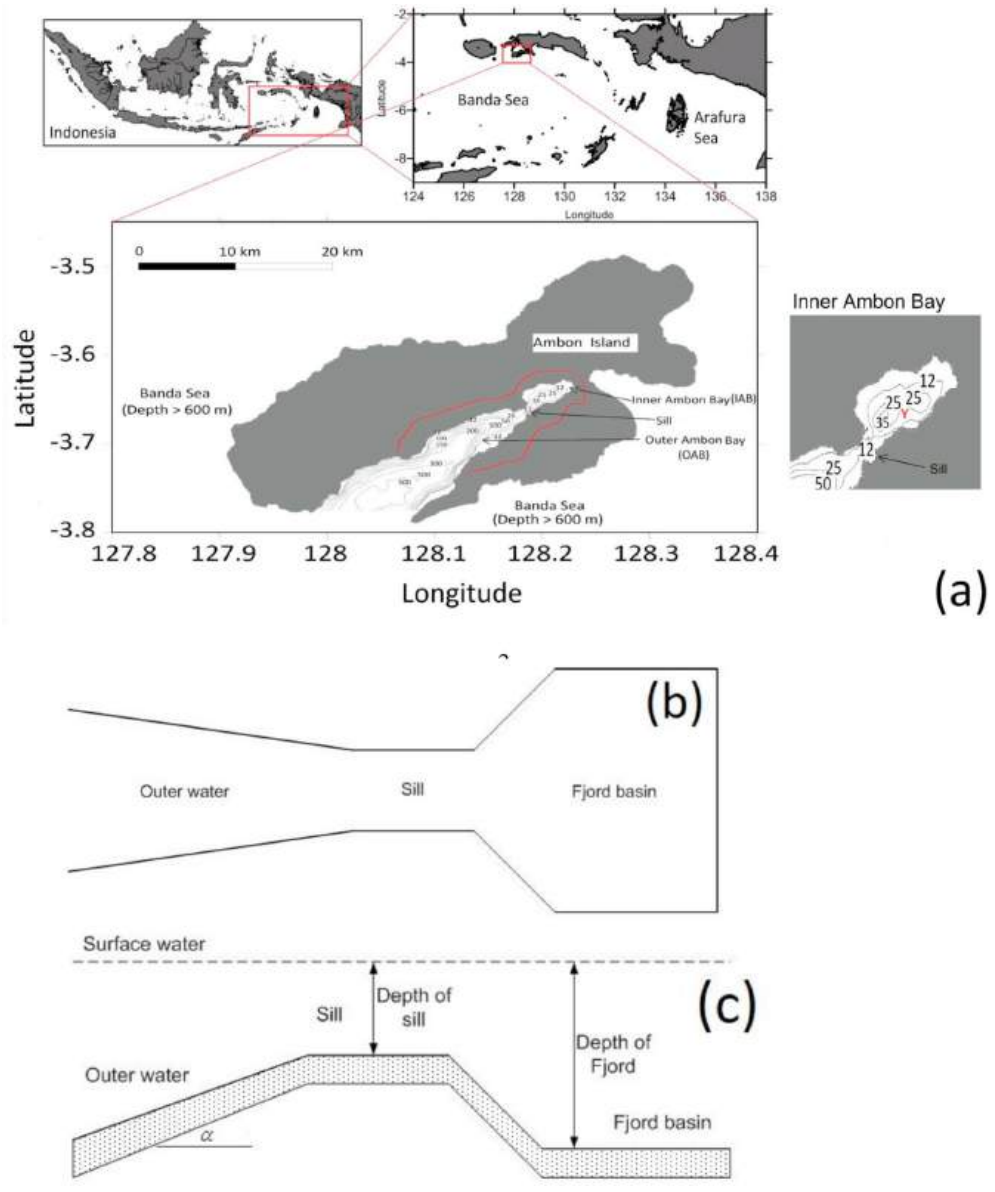

Fig. 1. (a) The geography of Ambon Bay located in Eastern Indonesian waters; bathymetric contours of Ambon Bay are in meters; red line in Ambon Island covers coastal areas of Ambon City. Inset: inner Ambon Bay (IAB) with its bathymetric contours in meters; Y in the inset represents area where maximum depth more than the sill depth (12 m). The schematic diagram of a fjord with single sill from (b) plan and (c) longitudinal views. (For interpretation of the references to color in this figure legend, the reader is referred to the Web version of this article.)

for Darwin Bay, which is, in addition, a well-protected conservation area.

There are profound scientific gaps in previous studies in Ambon Bay in terms of internal tidal dissipation and deep-water renewal. For example, regarding seasonal water stratification and tidal variability, internal tidal dissipation and its roles on deep-water renewal in Ambon Bay were only briefly investigated by previous studies using short-term longitudinal CTD casts (<3 days) (Rebert and Birowo, 1989; Wenno and Anderson, 1984). In contrast, seasonal- and tidal-based longitudinal CTD casts can reveal the seasonal and tidal variations in the supply of denser water at the sill likely causing the respective variations of deep-water renewal in IAB (Allen and Simpson, 1998; Gade and Edwards, 1980). Another analytical study (Anderson and Sapulete, 1982) only focused on steady-state density balances between the sill and IAB producing flushing inflow into IAB with the assumed constant density at the sill. This density assumption is rare in nature due to the variable supply of denser water at the sill (Gade and Edwards, 1980) following the potential episodic tidal upwelling events (Leichter et al., 2003, 2005; Wang et al., 2007).

Furthermore, the flushing capacity of IAB due to deep-water renewal seems to be inadequately investigated. Using a steady-state approach, Anderson and Sapulete (1982) predicted that the deep layer of IAB would be completely flushed in nine months. This estimation might be too long as the approach neglected high frequency forcing such as tidal cycles likely driving episodes of denser water from the sill slope into the fjord basin (Gade and Edwards, 1980). Another study (Pello et al., 2014) predicted a short flushing time of IAB (~14 days) based on a quasi-estuarine circulation mechanism (Bowden, 1983). This short flushing time is more likely due to estuarine-like transport only replenishing the surface volume of the fjord basin and hence, this surface water transport is not able to drive water circulation in the deep layer of IAB (Inall and Gillibrand, 2010; Stigebrandt, 1981).

In this current study, we addressed remaining scientific gaps by focusing on four substantial aspects. Firstly, we used data with far longer observational periods than the previous studies (e.g. 1–2 days (Rebert and Birowo, 1989; Wenno and Anderson, 1984)) to consider spring and neap tidal cycle measurements. Secondly, we observed the internal tidal-slope interaction in the spring and neap tides to investigate the variability of deep-water renewal due to tidal cycles. Thirdly, we measured the inflow transport of deep-water renewal along the sill and in IAB using bottom-mounted current meters within a spring-neap sequence. Fourthly, we quantified the flushing capacity of IAB due to deep-water renewal. These four aspects were conducted in both the easterly and transitional monsoonal seasons.

2. Physical description of Ambon Bay

The tropical fjord of Ambon Bay, eastern Indonesia, is characterized by a shallow sill (12 m) that separates IAB from OAB, which is a steady sloping outer section of Ambon Bay (Fig. 1a). The sill was formed from volcanic activity due to tectonically-generated active faults creating Ambon Island in the late Pliocene and the early Pleistocene (Honthaas et al., 1999; Lewerissa et al., 2018; Pownall et al., 2013). The sill is approximately 1 km long and 400 m wide with a cross-sectional area of c.a. 3700 m^2 (Pello et al., 2014). The steepness of the OAB slope ranges between 0.02 and 0.06 (source: Wenno and Anderson (1984) and Indonesian Navy's DISHIDROS bathymetric map) while the depth of IAB is, on average, 25 m (Fig. 1a).

IAB (volume: 0.22 km^3, Pello et al. (2014)) consists of the surface and deep layers. The surface layer has a thickness equal to the sill depth (12 m). The deep layer is located below the sill depth (Anderson and Sapulete, 1982) and occurs only in the region indicated by Y in the inset of IAB map (Fig. 1a). The volume of the deep layer of IAB is ~0.12 km^3.

Tidal cycles in Ambon Bay are a mixed semidiurnal. The spring tidal cycle in Ambon Bay produces a maximum flood-ebb water level difference of 2.5 m (spring tidal range) compared with 1.2 m for neap tidal cycle (van Oostenbrugge, 2003).

Ambon Bay experiences seasonal monsoonal winds that control its vertical stratification. The westerly monsoonal season (December to February) produces greater vertical stratification in OAB than the easterly monsoonal season (June to August) due to higher insolation and low rainfall (Putri et al., 2008; Tarigan, 1989; Tarigan and Wenno, 1991). In IAB, water density is controlled by freshwater inputs from rainfall producing low surface salinity (S = 25‰) in the easterly monsoonal season due to high rainfall, and moderate low salinity (S = 33‰) in the westerly monsoonal season. Underneath this low-density surface layer, oceanic water (S = 34‰) is found to be present throughout the year (Putri et al., 2008; Tarigan and Wenno, 1991). The presence of salty water in the deep layer of IAB is considered to be associated with deep-water supply from OAB (Wenno and Anderson, 1984). Periods between these two monsoons (i.e. transitional monsoonal seasons: March to May and September to November) are characterized by modest winds and warmer temperature comparable with the westerly monsoonal season (Tarigan, 1989; Tarigan and Wenno, 1991). Hence, water stratification is found to be the strongest in these transitional monsoonal seasons due to modest wind-driven surface mixing and intense insolation.

3. Data and methods

3.1. Internal tidal dynamics at sloping topography

The interaction between incoming internal tidal waves and sloping topography can be assessed using the criticality of internal tides, α/c. c, the ray slope of the incoming internal tides, is given by

$$c = \left(\frac{\sigma^2 - f^2}{N^2 - \sigma^2}\right)^{\frac{1}{2}}, \quad (1)$$

where N, f and σ are respectively near-bottom stratification frequency, the Coriolis frequency (i.e., f = sin (latitude)/12 cycle per hour, cph) and the internal wave frequency (e.g. 0.081 cph for semidiurnal tides) (Cacchione et al., 2002; Kumar et al., 2019; Lerczak et al., 2003; Subeesh and Unnikrishnan, 2016). For $\alpha/c < 1$ (sub-critical slope), internal tides will be reflected upward towards shallow depth; $\alpha/c > 1$, a supercritical slope, implies downward reflection of internal tides towards the deep ocean (Cacchione and Wunsch, 1974; Cacchione et al., 2002). For larger supercritical slope (α/c »1), however, the slope behaves as a wall which is likely to trap the incoming internal tides leading to local vertical mixing (Klymak et al., 2013; Legg and Klymak, 2008).

Sub-critical and supercritical slopes characterize the longitudinal density profiles during the interaction between internal tides and sloping topography. Sub-critical slopes will drive significant depression of isopycnal (i.e. the well-form internal lee waves) in the vertical density profiles leading to the establishment of internal surf towards shallow depths (Cacchione and Wunsch, 1974; Emery and Gunnerson, 1973). In contrast, for $\alpha/c > 1$, isopycnal is moderately depressed (hence, the absence of internal surf) (Cacchione and Wunsch, 1974). For α/c »1, sharply downward plunging isopycnals are expected to be evident around larger supercritical slopes (Legg and Klymak, 2008).

Sub-critical and supercritical slopes can drive upwelling. Sub-critical slopes are most likely to cause upwelling due to its characteristic to reflect incoming internal tides to shallow depths (Cacchione and Wunsch, 1974; Cacchione et al., 2002; Emery and Gunnerson, 1973; Kumar et al., 2019) and this upward reflection has been suggested to occur even with weak barotropic tidal flow (Baines, 1986; Subeesh and Unnikrishnan, 2016). Upwelling might also occur in supercritical slopes when barotropic tidal flow is intensified i.e. strong incoming barotropic flow has the potential to overshadow downwelling due to the downward reflection of incoming internal tides and thus, forcedly pumps deep-water at the slope to shallow depths.

3.2. CTD casts

CTD casts were conducted along the longitudinal section of Ambon Bay from OAB to the sill (black circles in Fig. 2a; Alec Electronics Japan, salinity and temperature accuracies: ± 0.03‰ and ±0.02 °C). Cast sites on the slope of OAB (S1 to S9, Fig. 2b) were set to be perpendicular to bathymetric contours (Fig. 1a) aiming to observe the interaction between internal tidal waves and the slope. This approach follows previous observational studies of internal tides associated with the bottom slope (Alford et al., 2014; Bruno et al., 2006; Sandstrom and Oakey, 1995; Staalstrøm et al., 2014). The CTD casts in OAB were mostly conducted during the flood tide when the expected collision between incoming internal tides and the slope occurs. Likewise, the flood tide CTD cast stations along the sill (i.e. C1–C5 in Fig. 2b) were designed to observe the thickness of deep-water inflow (i.e. the depth of upwelled water at the sill).

CTD casts in OAB were timed with the turn of the tide to best capture interactions of tides with the slope following the technique of Alford et al. (2014). CTD casts started from the offshore Ambon Bay (S9) at the time water elevation just started increasing from its minimum value (low tide) so that CTD stations at the slope close to the sill and at the sill were reached by the time the maximum flooding tidal flow occurred. In the Ambon Bay tidal pattern, this period of rapid change in water elevation within the flood cycle always occurs before the peak water elevation. This timing aimed to capture the most energetic conditions of the breaking of internal tides or the reflection of internal tides at the slope. This CTD cast scheme also has the potential to capture the maximum thickness of the deep-water inflow at the sill since the deep-water inflow is intensified during the maximum tidal flow (Gade and Edwards, 1980). Harmonic-derived water elevation predictions for Ambon Bay (DISHIDROS tidal table) were used to guide these tidal timing-based CTD casts.

Seasonally significant contrasts in internal tidal dissipation at the OAB slope were analyzed by considering periods of weakest and strongest stratification conditions in OAB. For the weakest water stratification condition, CTD casts were conducted in July 2019 during the easterly monsoonal season. For the strongest water stratification condition, measurements were taken in October 2019 during the transition from the easterly to westerly monsoon when winds are lightest. Regarding tidal cycles, CTD casts were conducted during the spring tide, that is, 17–21 July 2019 and 17–22 October 2019 for both the easterly and transitional monsoonal seasons, respectively, and 25–27 July 2019 and 9–11 October 2019 for the neap tide measurements during the respective seasons. CTD casts along the sill (C1–C5, Fig. 2b) with the same flooding timing to those for the spring and neap tidal cycles were also conducted during the periods between the spring and neap tide (i.e. 22-24 July 2019 for the easterly monsoonal season and 12–16 October 2019 for the transitional monsoonal season) in attempts to increase the probability to observe the thickness of deep-water inflow along the sill.

In addition, CTD casts were taken on ebb tides so that a tidally-averaged vertical density profile in OAB could be calculated. This steady-state vertical density was compared with the flooding tidal vertical density profiles during spring and neap tides in order to analyze the degree of isopycnal depression (i.e. internal lee waves) in these tidal cycle towards the steady state condition.

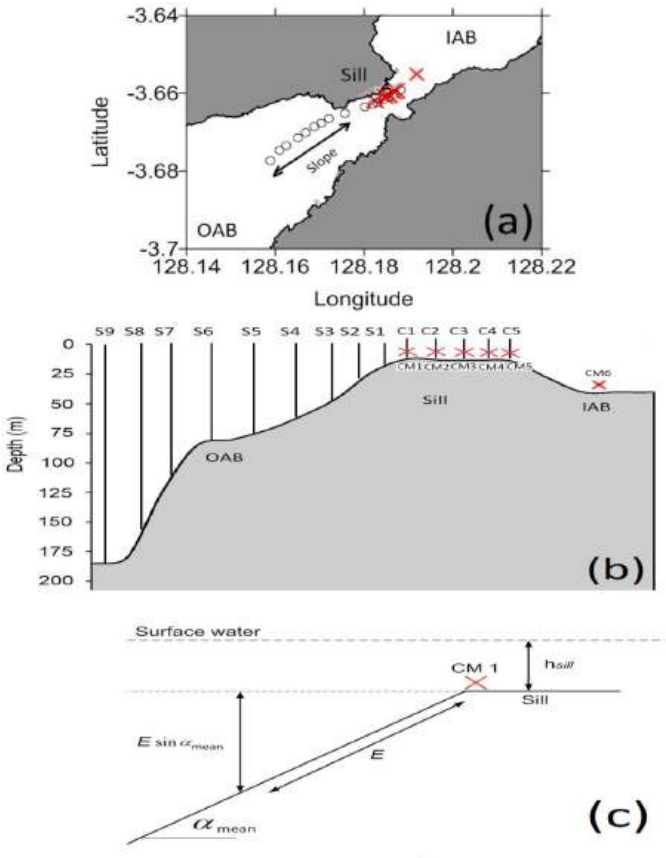

Fig. 2. (a) CTD stations, ○, and bottom-mounted current meters, ×, which are located on the sill and IAB; (b) Longitudinal section of instrument sections with S1–S9 and C1–C5 indicating CTD stations (i.e. (○) in Fig. 2a) located at the OAB slope and the sill, respectively; × in Fig. 2a labelled CM1-CM6. (c) Schematic diagram to infer the original depth of deep-water reaching the sill due to tidal upwelling using tidal excursion, *E*.

3.3. Current meter moorings

3.3.1. Deep-water inflow measurements

Five bottom-mounted current meters equipped with temperature sensors (i.e. Marotte-tilt drag current meters (Marchant et al., 2014)) were deployed along the sill (CM1 to CM5, Fig. 2b) and one in IAB (CM6, Fig. 2b) to measure the velocity and temperature of deep-water inflow at the seabed. The bottom-mounted current meters were deployed for a full spring-neap cycle (i.e. 2 weeks) (Edwards et al., 1980; Gade and Edwards, 1980).

In addition to direct current measurements of deep-water inflow, we also introduced a new technique to measure the speed of deep-water inflow in Ambon Bay using the temperature sensors in the current meters. The speed of deep-water inflow was estimated by looking at the time lag between changes in temperature due to the passing of deep-water inflow between sensors at the offshore sill (CM1) and in IAB (CM6).

3.3.2. Tidal excursion to predict depths from which water upwells to the sill

Tidal excursion, *E*, can be used to determine from what depth water is upwelled to the sill. From Fig. 2c, larger tidal excursion means that water comes from a deeper layer. Tidal excursion is, mathematically, expressed as

$$\mathrm{E} = \int_{t_1}^{t_2} u(t)\, dt, \tag{2}$$

where t_1 and t_2 are respectively the beginning and the end of the flood tide and u is the ocean current speed measured at the offshore sill (CM1, see Fig. 2b and c). α_{mean} in Fig. 2c is the average slope from S1 to S9. This application of tidal excursion is possible by assuming that upwelled water flows along the slope due to internal surf (Cacchione and Wunsch, 1974; Emery and Gunnerson, 1973) with a constant cross-sectional area.

3.4. The use of thermal-tidal excursion to analyze the influx of deep-water inflow across the Ambon Bay sill

The influx of deep-water inflow across the sill of Ambon Bay was assessed by so-called thermal-tidal excursion, $E_{plume} = [T_o - \overline{T}_{dw}]\ \bar{u}_p\ \Delta t_p$ (^oC m). The thermal-tidal excursion was utilized following the extension of deep-water plumes along the sill more likely to be controlled by the density difference between the plume and the sill water mass (i.e. $[T_o - \overline{T}_{dw}]$) (Benjamin, 1968) and by the tidal excursion ($\bar{u}_p\ \Delta t_p$). $\bar{u}_p$ is the averaged flooding currents during the deep-water inflow events measured at CM1 which is the starting point of plumes and Δt_p is the duration of the supply of deep-water from CM1. $\overline{T}_{dw}$ is the average temperature of the arrived deep-water at the sill (i.e. at CM1) within Δt_p and T_o is the normal bottom temperature at the sill in the absence of deep-water inflow (i.e. typically during ebb tides; Allen and Simpson, 1998). The characteristic depth from which the water at temperature $\overline{T}_{dw}$ arrives can be determined from profiles of temperature on the slope. A value of E_{plume} will be obtained to be a threshold condition that by exceeding it, deep-water plumes are likely to arrive at the inshore sill.

3.5. Logistical constraints during field-measurements

A major inevitable constraint in CTD measurements in this current study is marine traffic in Ambon Bay; hence, safety dictated that we only conducted CTD casts for the flood and ebb tides in daytime. Daytime CTD measurements reduce likelihood to capture deep-water renewal events (i.e. measuring the thickness of deep-water inflow along the sill) and hence, there were few modifications during the fieldwork campaign. For example, from the bottom-mounted current meters at the sill, most of the deep-water renewal events (i.e. observed cooler water) occurred in the nighttime in July 2019 except on July 26, 2019 with all deep water renewal events occurring in the nighttime in October 2019. The tendency of nighttime deep-water renewal events in Ambon Bay prevents daytime CTD casts from capturing the thickness of deep-water inflow along the sill. Thus, we deployed HOBO temperature loggers at the depths of 9 m and 6 m besides the temperature logger from CM3 at the seabed (at 12 m) in 30 October – November 13, 2019 to capture the thickness of deep-water inflow in the transitional monsoonal season. Table 1 summarizes all oceanographic measurements in this study, showing the information on the initial and modified observational scenarios.

Table 1
Metadata of oceanographic measurements in this study. The locations of CTD cast stations (i.e. S1–S9 and C1–C5) and current meters (CM1-CM6) are shown in Fig. 2a and b. CTD type: Compact-CTD Alec electronic; current meter type: Marotte-tilt drag current meters; temperature loggers: HOBO U22-001 data logger.

Measurement scenarios	Seasonal condition	Observation method	Period of measurements
Initial observation	Easterly monsoonal season	Daily CTD casts in flood and ebb conditions	Stations S1–S9 Spring tide: 17–21 July 2019 Neap tide: 25–27 July 2019 Stations C1–C5 17–July 27, 2019
		Bottom-mounted current meters deployed at the sill (CM1-CM5, at 12 m) and in IAB (CM6, at 37 m)	CM1-CM5: July 12, 2019, 10:00–July 30, 2019, 12:00 CM6: July 13, 2019, 12:00–July 29, 2019, 12:00
	Transitional monsoonal season	Daily CTD casts in flood and ebb conditions	Stations S1–S9 Spring tide: 17–22 October 2019 Neap tide: 9–11 October 2019 Stations C1–C5 9–22 October 2019
		Bottom-mounted current meters deployed at the sill (CM1-CM5, at 12 m) and in IAB (CM6, at 37 m)	CM1-CM5: October 3, 2019, 8:00–October 24, 2019, 10:00 CM6: October 4, 2019, 10:00–October 25, 2019, 12:00
Modified observation	Transitional monsoonal season	CM3 at the bottom coupled with two additional temperature loggers at water column of the sill (depths of 9 m and 6 m)	October 29, 2019, 10:00–November 13, 2019, 9:00

4. Results

This result section mainly reports the characteristics of internal tidal waves in the OAB slope and the evidence of deep-water inflow at the sill and IAB. Sub-section 4.1 describes seasonal characteristics of internal tides at the OAB slope. Sub-section 4.2 presents the evidence of tidal upwelling at the entrance of the sill due to internal tidal dynamics. Following that are the seasonal characteristics of deep-water inflow along the sill (Sub-section 4.3). Sub-section 4.4. presents the evidence of deep-water renewal in IAB and the estimation of flushing rate of IAB due to seasonal deep-water renewal.

4.1. Seasonal characteristics of internal tides in Ambon Bay

Vertical density of OAB is seasonally variable. OAB is less stratified in the easterly monsoonal season (vertical temperature gradient, dT/dz: on average, 0.02 $^\circ$C/m, surface-bottom temperature difference: ~5 °C, Fig. 3a) than in the transitional monsoonal season (dT/dz: on average, 0.06 $^\circ$C/m, surface-bottom temperature difference: ~10 °C, Fig. 3b). Note, a spring/neap, flood/ebb-tidally averaged temperature was used for a steady-state vertical density profile (Fig. 3a and b) due to insignificant changes caused by salinity in the vertical density in OAB (Putri et al., 2008).

The seasonal vertical stratification (Fig. 3a and b) and bottom slope, α (Fig. 3c), control the seasonal criticality of internal tides in OAB (Fig. 3c). During easterly monsoonal season, slopes at S1 – S5 are sub-critical ($\alpha/c < 1$) whereas only S1 is sub-critical in the transitional monsoonal season. The greater fraction of the OAB slope that is sub-critical in the easterly monsoonal season is caused by less water stratification in OAB compared to the transitional monsoonal season. S6 to S9 are supercritical in both seasons with less supercritical slopes found during the easterly monsoonal season. In addition, larger supercritical slopes ($\alpha/c \gg 1$) are evident at S7 and S8 in both seasons due to their steep bathymetric slopes ($\alpha > 0.1$).

The effects of seasonal α/c on internal tides in Ambon Bay are shown in Fig. 4. More sub-critical regions ($\alpha/c < 1$) in the easterly monsoonal season particularly between S1 and S6 (Fig. 3c) caused most evident internal surf in this location (i.e. Box 1 in Fig. 4a and Box 3 in Fig. 4b). These internal surf signatures were absent in the transitional monsoonal season (Fig. 4c and d) when supercritical regions ($\alpha/c > 1$) predominate in this location (Fig. 3c). Larger supercritical slopes ($\alpha/c \gg 1$) at S7 and S8 produced more sharply downward plunging isotherms particularly in the easterly monsoonal season (i.e. Box 2 in Fig. 4a and Box 4 in Fig. 4b) compared to the transitional monsoonal season (Fig. 4c and d).

The amplitude of internal tide in the slope of OAB is affected by seasonal water stratification and the tidal cycles. Weak water stratification in the easterly monsoonal season produces larger amplitude of internal lee waves (i.e. the isothermal depression) with amplitude as much as ~50 m (i.e. at S7 in Fig. 4b) compared to that during strong

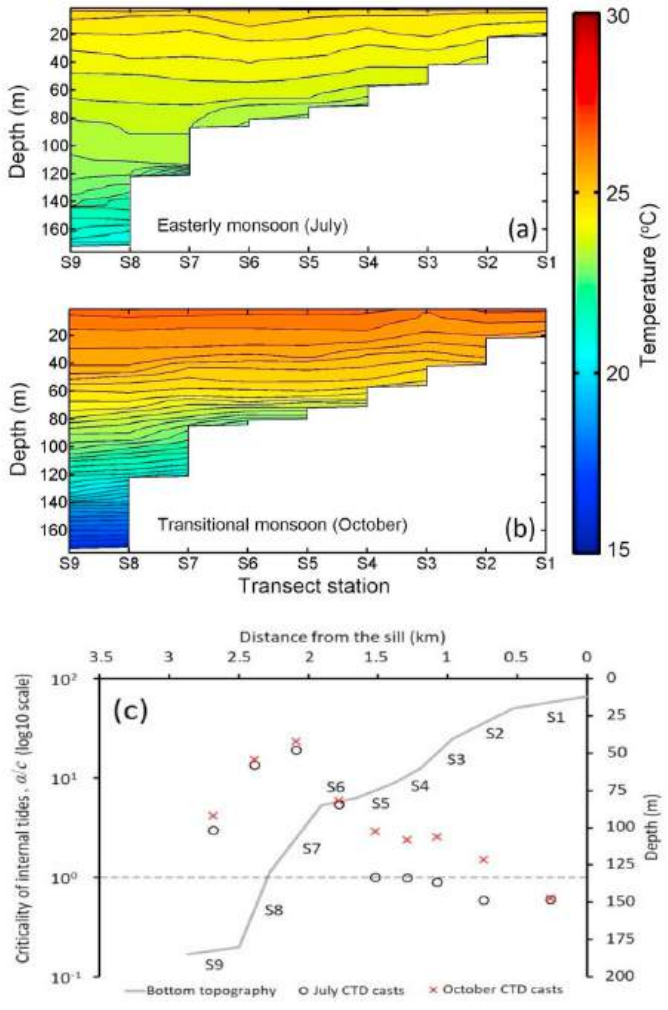

Fig. 3. Temperature profiles of OAB averaged for all spring/neap, flood/ebb conditions in (a) the easterly monsoonal season (July 2019) and (b) the transitional monsoonal season (October 2019); Contour step is 0.25 °C. (c) CTD cast locations on the OAB slope and the criticality of internal tides, α/c, for the easterly monsoonal season, ○, and for the transitional monsoonal season, ×. Horizontal dashed line at $\alpha/c = 1$ was drawn to distinguish the regions of subcritical slope ($\alpha/c < 1$) and supercritical slope ($\alpha/c > 1$).

water stratification in the transitional monsoonal season (maximum amplitude of 20 m at S7, in Fig. 4d). Additionally, spring tides drive larger internal tidal amplitude than during the neap tide in both easterly (~50 m in Fig. 4b *cf.* ~40 m in Fig. 4a) and transitional (20 m in Fig. 4d *cf.* ~10 m in Fig. 4c) monsoonal seasons.

4.2. Tidal upwelling at the sill of Ambon Bay

Tidal upwelling events in Ambon Bay (i.e. deep water from the OAB slope reaching the sill) in the easterly and transitional monsoonal seasons are represented by sudden reductions of temperature (Roman numerals in Fig. 5a and b) recorded at the offshore sill section (CM1). Tidal upwelling only occurred during flooding tides with upwelled water indicated by $T < \sim 24$ °C for easterly monsoon season and $T < \sim 25$ °C for transitional monsoonal season (Fig. 5c and d). Note, harmonic-derived water elevation predictions (light blue lines) were plotted along with the observations of bottom temperature (red line) and bottom current speed (black line) in Fig. 5a and b to indicate the tidal cycles during the measurements.

In general, tidal upwelling is more frequent and more significant in terms of the reduction in water temperature at the sill in the spring tide than in the neap tide for both the easterly and transitional monsoonal seasons (Fig. 5a and b). The significance of the spring tide in driving tidal upwelling in both seasons is related to larger tidal excursion, E, in the spring tide that causes cooler water from the OAB slope to arrive at the bottom layer of the sill following a significant correlation ($R^2 > 0.7$) between E and the minimum bottom temperature recorded at the sill (i.e. CM1, Fig. 5e and f). Larger values of E occurred less frequently during neap tides such as on July 26, 2019 (XII in Figs. 5a) and July 28, 2019 (XIII in Fig. 5a).

Larger values of tidal excursion driving tidal upwelling is due to longer flooding tide, that is, when bottom currents are directed into IAB (flood) even while surface elevation falls (ebb), occurring in each monsoonal season (14–20 July 2019, 26 and July 28, 2019, Fig. 5a; 04–07 October 2019 and 19–21 October 2019, Fig. 5b). These extended periods of bottom water intrusion lasted up to 17 h and result from strong flow of tidal floods coupled with weak ebb tides between lower high water and higher low water; these weak ebb tides are indicated by the falls of surface elevation that are still above mean sea level (Fig. 5a and b).

The estimation of depth from which water is upwelled to the sill based on Fig. 2c is found to roughly agree with the observed temperature from CTD casts (Fig. 5g). For the easterly monsoonal season, deep-water masses arriving at the sill (i.e. $T < 24$ °C, Fig. 5c) with temperatures of 23 °C and 22 °C are likely to originate from depths approximately 140 m and 180 m, respectively. For the transitional monsoonal season, deep-water masses (i.e. $T < 25$ °C, Fig. 5d) with temperatures of 24 °C and 23 °C are likely to originate from depths of 85 m and 110 m, respectively.

4.3. Deep-water inflow along the sill of Ambon Bay

Deep-water inflow along the sill of Ambon Bay was well-observed by oceanographic measurements in this study (Fig. 6). For instance, in the easterly monsoonal season, CTD casts on the sill captured a cool, salty deep-water plume ($T < 24$ °C in Fig. 6a and $S > 33.95$‰ in Fig. 6c) along the bottom of the sill. Likewise, in the transitional monsoonal season, deep-water inflow along the sill is represented by cooler water at the near seabed (i.e. $T < 25$ °C, Fig. 6b). Note, daytime CTD casts in the transitional monsoonal season did not capture deep-water inflow events, which occurred only at night due to the timing of tides. As such, data from moored temperature loggers are shown (Fig. 6b); these datasets were obtained after the CTD campaigns and are indicated by the modified observation in Table 1. In addition, the thickness of deep-water inflow along the sill is roughly constant in both easterly and transitional monsoonal seasons (i.e. 5 ± 1 m, Fig. 6).

The arrival of deep-water plumes at the inshore sill (CM5) from the offshore sill (CM1) is controlled by the thermal-tidal excursion, $E_{plume} = [T_o - \overline{T}_{dw}]\, \bar{u}_p\, \Delta t_p$. In general, deep-water inflows not reaching the inshore sill in the easterly monsoonal season (II, VI, IX, X and XI, Fig. 7a) and the transitional monsoonal season (XVII, XIX, XX and XXI, Fig. 7b) are associated with E_{plume} smaller than 1000 °C m (Fig. 7c). We therefore use 1000 °C m as the threshold value of thermal-tidal excursion controlling the influx of deep-water inflow across the sill of Ambon Bay. Note, T_o was 24 °C and 25 °C for the easterly and transitional monsoonal seasons, respectively, indicating the normal bottom temperature at the sill in the absence of deep-water plume (see Fig. 5c and d) with $\overline{T}_{dw}$ less than these T_o values in the respective seasons.

Contributions to the thermal-tidal excursion larger than 1000 °C m from the two components (i.e. tidal excursion, $\bar{u}_p\, \Delta t_p$, and deep-water/sill density difference, given by $[T_o - \overline{T}_{dw}]$) revealed different patterns for the two seasons (boxes in Fig. 7d). In the easterly monsoonal season (□ in Fig. 7d), the variation in the thermal-tidal excursion was predominated by changes in tidal excursion. In contrast, this variation during the transitional monsoonal season (○ in Fig. 7d) was controlled by changes in density difference.

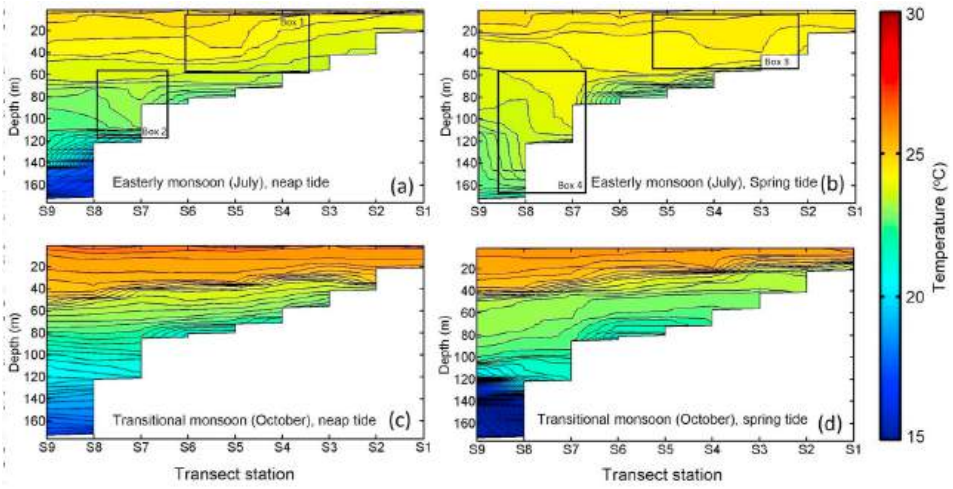

Fig. 4. Longitudinal temperature profiles in the easterly monsoonal season during (a) neap tides and (b) spring tides; (c) and (d) are similar to (a) and (b) but for the transitional monsoonal season. Boxes 1 and 3 indicate the locations of internal surf while boxes 2 and 4 show more sharply downward plunging isotherms around steep physical slopes at S7 and S8.

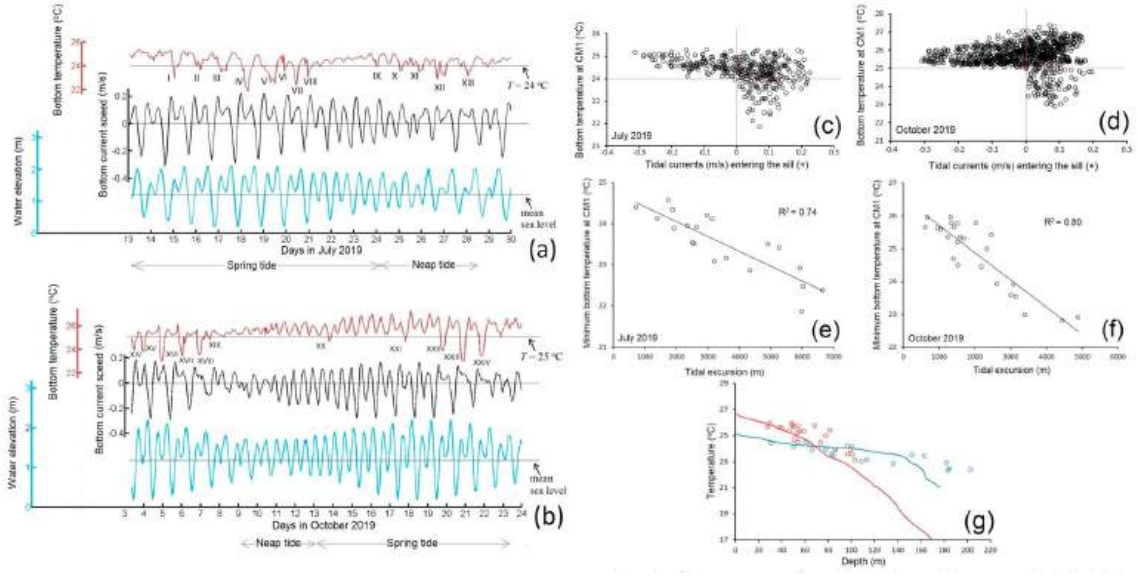

Fig. 5. Time series of bottom temperature (° C, red line) and bottom tidal current speed (m/s, black line) at the offshore sill (CM1) along with water elevation prediction (m, blue line) in (a) July 2019, the easterly monsoonal season and (b) October 2019, the transitional monsoonal season. The axis color follows the color of line plot (e.g. light blue axis for water elevation). Positive values of tidal current speed indicate water flowing into the sill. Roman numerals indicate the sequence of tidal upwelling events throughout measurements. Water elevation is harmonic analysis which was obtained from DISHIDROS tidal table. Scatter plots of bottom tidal current speed vs bottom temperature at CM1 for (c) July 2019, the easterly monsoonal season and (d) October 2019, the transitional monsoonal season. Estimated tidal excursion, *E*, derived from measured velocity at current meter CM1 plotted against the minimum bottom temperature recorded at CM1 during each flooding tide in (e) July 2019, the easterly monsoonal season and (f) October 2019, the transitional monsoonal season. (g) Water temperature at CM1 during tidal upwelling against inferred original depth of tidally-upwelled water (circles) during the easterly monsoonal season (blue circles) and the transitional monsoonal (red circles). Lines show the vertical temperature profile from CTD casts at S9 that are spring-neap, flood-ebb averaged (Fig. 3a and b). (For interpretation of the references to color in this figure legend, the reader is referred to the Web version of this article.)

A regression model was developed to quantify the dependence of the two components of thermal-tidal excursion (i.e. $E_{plume} = \beta_o + \beta_1[\bar{u}_p\, \Delta t_p] + \beta_2[T_o - \overline{T}_{dw}]$) of deep-water plumes that propagate across the sill ($E_{plume} > 1000$ °C m) in the different seasons. The appropriateness of separating the components of the thermal-tidal excursion is demonstrated by the high correlation of E_{plume} ($R^2 > 0.94$) calculated from the original product compared with the regression analysis (Fig. 7e, Table 2). Therefore, the regression analysis (Table 2) supports the patterns in Fig. 7d to reveal that upwelled water successfully crossing the sill is controlled by the tidal excursion of the deep-water plume in the easterly monsoonal season and by the deep-water/sill density difference in the transitional monsoonal season.

4.4. Deep-water renewal in inner Ambon Bay

The evidence of deep-water reaching the bottom of IAB is shown in Fig. 8a and b. In general, the deep-water masses successfully crossing the sill ($E_{plume} > 1000$ °C m in Fig. 7c) subsequently sink into the seabed of IAB (Fig. 8a and b). The signatures of deep-water renewal events in IAB are mostly represented by rapid reductions of bottom temperature except one event in the easterly monsoonal season (i.e. VIII as shown by red arrow in Fig. 8a) indicating that the presence of deep-water in IAB

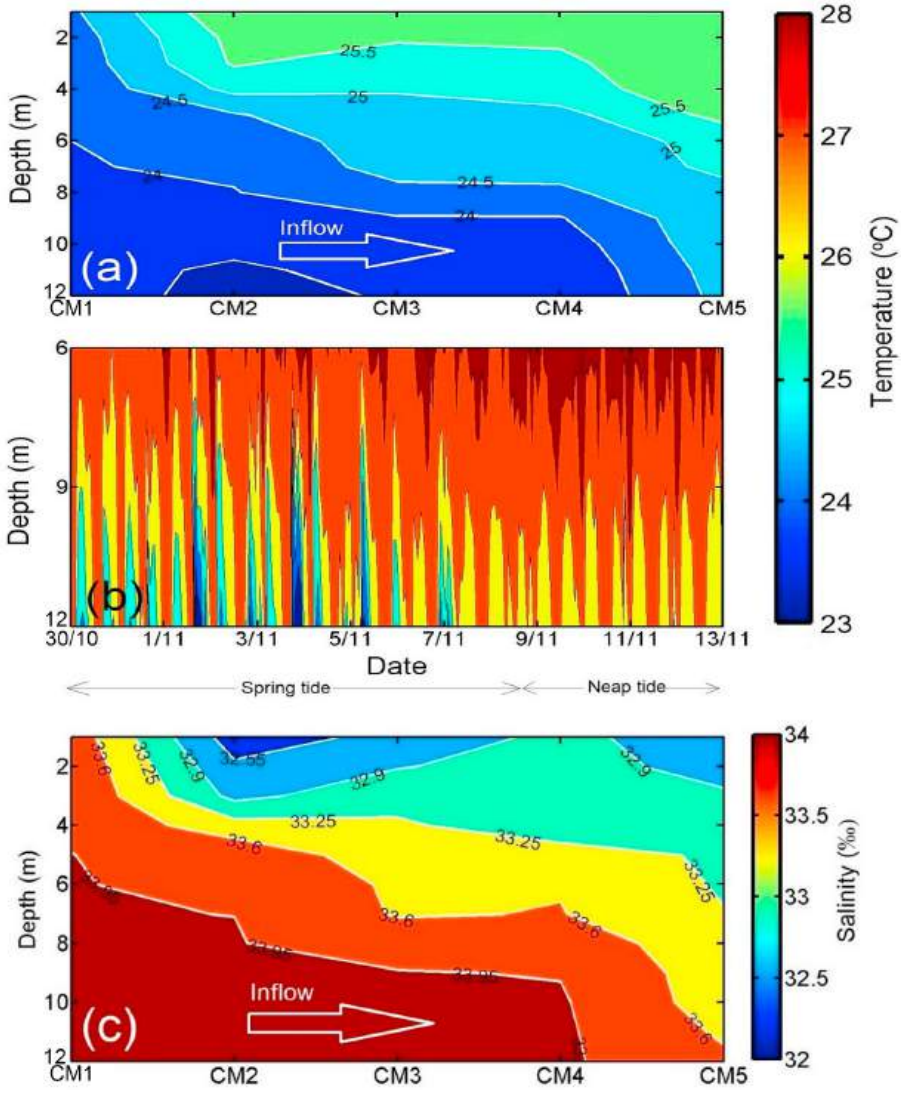

Fig. 6. (a) Longitudinal profiles of temperature at the sill of Ambon Bay with CTD casts conducted at the locations of moored current meters on July 26, 2019 during the flood tide (see Fig. 2b for the locations of moored current meters). (b) Temporal evolution of water temperature within 6 m of the seabed at the mid-section of the sill (CM3) over a spring-neap sequence (30 October – November 13, 2019). These data were obtained from the temperature sensor at CM3 at the seabed (12 m) and HOBO temperature loggers at the depths of 9 m and 6 m. (c) Similar to Fig. 6a but for salinity.

slows the relaxation of the temperature of IAB. Note, the delayed deployment of CM6 in the transitional monsoonal season (i.e. on October 4, 2019) meant that the deep-water renewal in IAB on October 3, 2019 (i.e. XIV and XV) was not observed.

The inflow velocity as measured by the current meter directly and from the temperature time lag method always agree within ~13% with the time lag method almost always slightly higher (Fig. 8c). In general, the velocity of deep-water inflow ranges between 0.05 m/s and 0.1 m/s (Fig. 8c). Note, we only considered CM6 in IAB (at 35 m depth) to be the direct measurement of deep-water inflow in this study since the remaining current meters at the sill (CM1-CM5, at 12 m depth) are subject to noise due to the effects of tides in shallow depth.

The degree of flushing process in the deep layer of IAB (volume: 0.12 km^3) was represented by the volume proportion of this layer, flushed by each pulse of deep-water renewal (Table 3). For the easterly monsoonal season, a series of pulses of deep-water inflow within a spring-neap sequence (i.e. 14-28 July 2019, see Fig. 5a) produced a total inflow volume of 0.09 ± 0.02 km^3 which is approximately 80% volume of this deep layer. For the transitional monsoonal season, this spring-neap sequence (i.e. 9-24 October 2019, see Fig. 5b) replenished roughly 40% volume of the IAB deep layer (total inflow volume: 0.05 ± 0.01 km^3).

5. Discussion

5.1. Seasonal characteristics of internal tides in Ambon Bay

Seasonal water stratification in OAB is affected by seasonal atmospheric conditions over Ambon Bay. Weak water stratification in OAB in the easterly monsoonal season (Fig. 3a) is due to lower insolation (i.e. high columnar cloud liquid water: 0.3 mm) and intense surface mixing due to easterly monsoonal winds (Tarigan, 1989). In contrast, water stratification is stronger in the transitional monsoonal season and is related to lower columnar cloud liquid water (0.04 mm) and modest winds (Tarigan, 1989) (cloud liquid water data source: http://www.remss.com/missions/amsr/).

The seasonal variation in the criticality of internal tides, α/c, in the OAB slope (Fig. 3c) is likely to control tidal upwelling in Ambon Bay. More sub-critical regions ($\alpha/c < 1$) at the OAB slope in the easterly monsoonal season highly promote the upward reflection of incoming internal tides to shallow depths as demonstrated by most evident internal surf (Fig. 4a and b) (Cacchione and Wunsch, 1974; Cacchione et al., 2002; Emery and Gunnerson, 1973; Kumar et al., 2019). This condition thus encourages tidal upwelling. In contrast, the predominant supercritical regions ($\alpha/c > 1$) in the OAB slope in the transitional monsoonal season has the potential to prevent tidal upwelling as incoming internal tides are mostly reflected back to the deep ocean

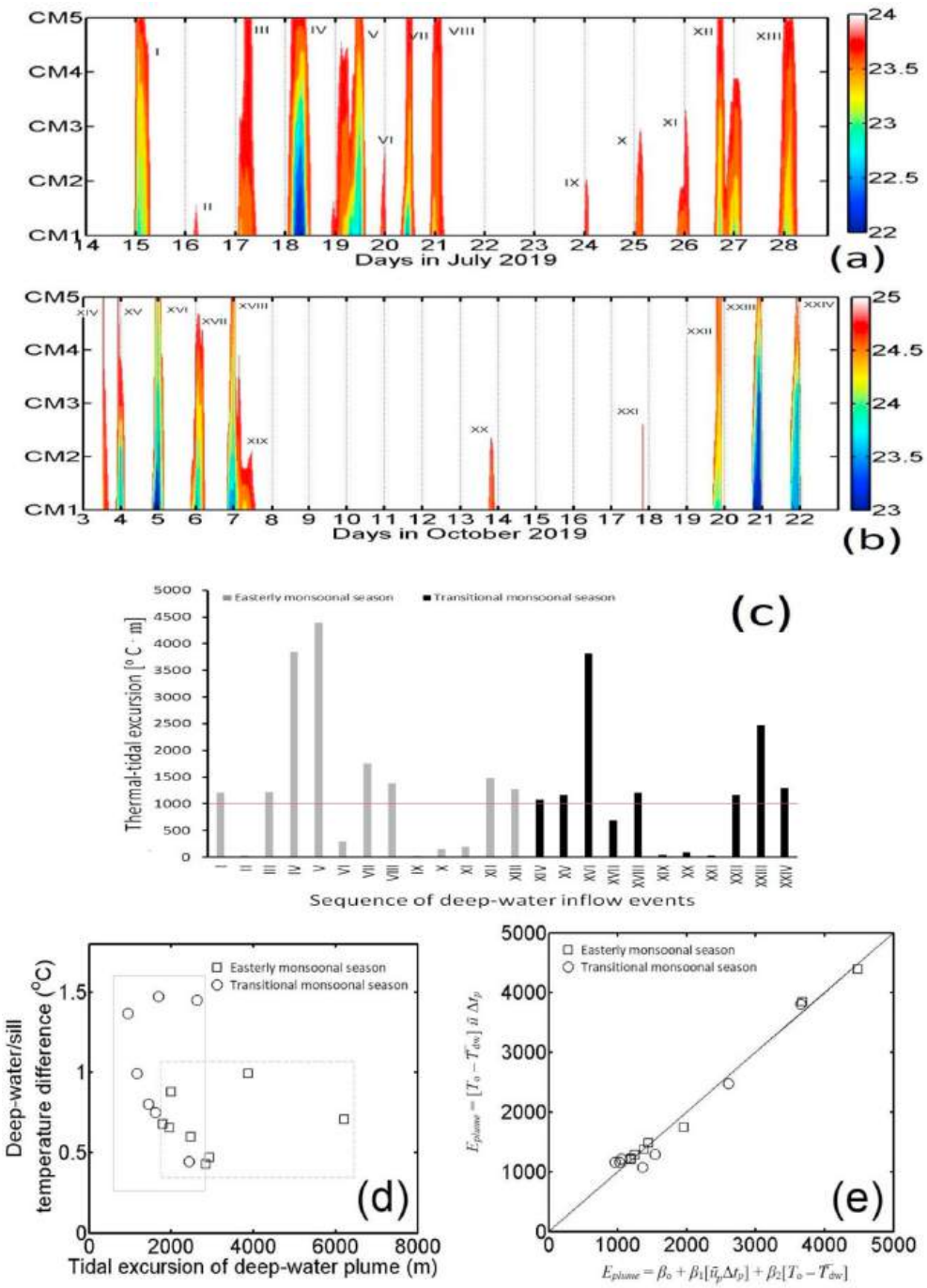

Fig. 7. Spatial and temporal evolutions of bottom temperature measured along the sill in (a) the easterly monsoonal season and (b) the transitional monsoonal season; Roman numerals in these figures recall the tidal upwelling events previously shown in Fig. 5a and b. Note, observed temperatures larger than deep-water temperature in the easterly monsoonal season ($T < 24$ °C, Fig. 5c) and in the transitional monsoonal season ($T < 25$ °C, Fig. 5d) are colored white so that, the extent of deep-water plume along the sill is apparent. (c) Thermal-tidal excursion, E_{plume}, of deep-water inflow events (Roman numerals) during the easterly monsoonal season (grey) and the transitional monsoonal season (black). Red line indicates $E_{plume} = 1000$ °C m. (d) Tidal excursion (m) vs deep-water/sill temperature difference (°C) for the deep-water plumes reaching the inshore sill ($E_{plume} > 1000$ °C m). (e) E_{plume} estimated using multivariate linear regression (x axis) vs the original estimation of E_{plume} (y axis); only $E_{plume} > 1000$ °C m was used in this plot indicating the arrived deep-water at the inshore sill with (□) and (○) representing E_{plume} for the easterly and transitional monsoonal seasons, respectively. (For interpretation of the references to color in this figure legend, the reader is referred to the Web version of this article.)

Table 2
Regression coefficients of multivariate linear regression analysis to determine which drivers controlling the arrival of deep-water plume at the inshore sill.

Components of thermal-tidal excursion	Regression coefficients	
	The easterly monsoonal season ($R^2 = 0.99$)	The transitional monsoonal season ($R^2 = 0.95$)
$[\bar{u}_p\ \Delta t]$	0.82	0.62
$[T_o - \overline{T}_{dw}]$	0.45	0.84

(Cacchione and Wunsch, 1974; Cacchione et al., 2002).

The roles of water stratification and tidal flow on the amplitude of internal tidal waves in Ambon Bay are in agreement with previous studies. For instance, weak water stratification in the easterly monsoonal season drives larger isothermal depression compared to that in the transitional monsoonal season (Fig. 4), similar to the summer-winter comparison in Red Sea (Guo et al., 2016). The large amplitude of internal waves due to strong ocean flow, as in the spring tide in this study, is consistent with the numerical studies of Legg and Klymak (2008) and Guo et al. (2016).

5.2. Tidal upwelling in Ambon Bay and its connection with seasonal internal tidal dynamics in Ambon Bay

The prediction of the original depth of deep-water reaching the sill in this current study is generally comparable with previous values. In a single cross-sectional observation in the easterly monsoonal season

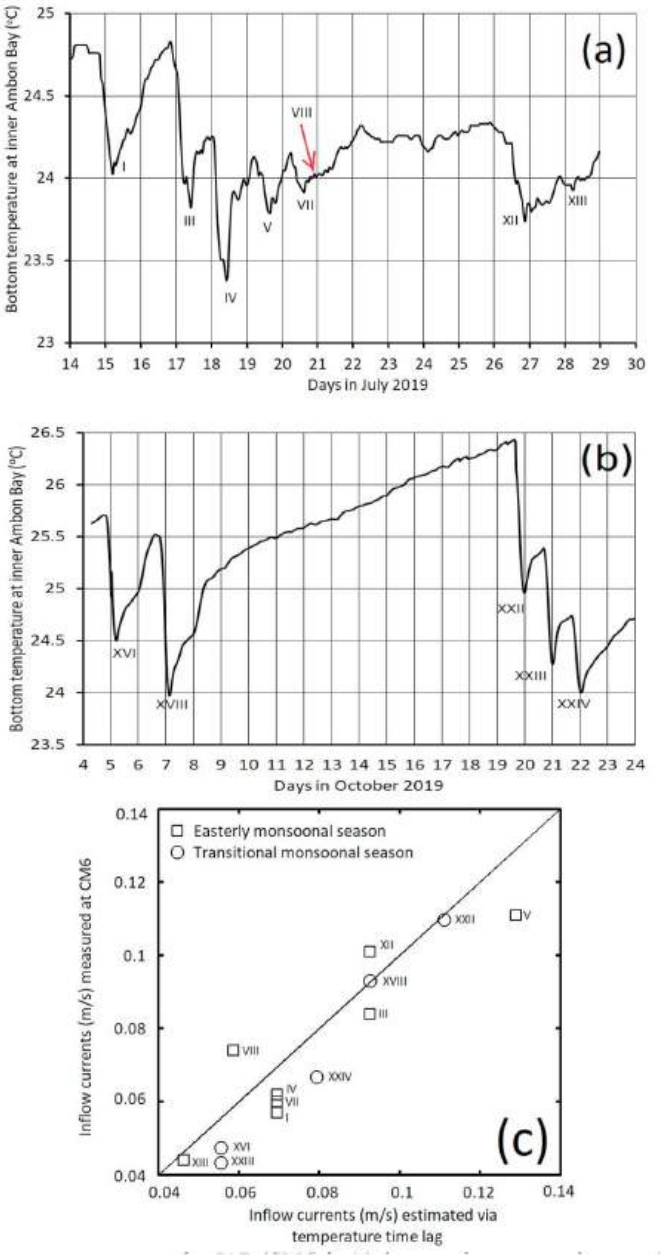

Fig. 8. Bottom temperature measured at IAB (CM6) in (a) the easterly monsoonal season (July 2019) and (b) the transitional monsoonal season (October 2019). Roman numerals in Fig. 8a and b indicate arrived deep-water masses at inner Ambon Bay which can be tracked back when they moved along the sill (Fig. 7a and b). Note, the delayed deployment of CM6 (i.e. on October 4, 2019) caused the absent observation of deep-water renewal on October 3, 2019. (c) Observed speed of deep-water inflow in IAB (CM6) plotted against deep-water inflow speed estimated by temperature time lag with associated deep-water renewal events (Roman numerals).

(August 13, 1982), Wenno and Anderson (1984) observed that, during the flood tide, deep-water with temperature of 23.5 °C had upwelled from depths around 70 m–85 m in OAB to reach the sill and subsequently sink into IAB. Here, for the easterly monsoonal season, bottom water at the sill with temperature of 23.5 °C is predicted to be originally from around 90 m in OAB (Fig. 5g).

The occurrence of tidal upwelling in Ambon Bay appears to be dependent on the seasonal dynamics of internal tides working hand-in-hand with the neap-spring tidal cycle. Previous studies (Baines, 1986; Subeesh and Unnikrishnan, 2016) had suggested that the generation of

Table 3
The volume discharge rate (m^3/s) of deep-water inflow and associated volume (km^3) of deep-water supplied into IAB. The volume discharge rate (m^3/s) was estimated using the inflow rate at CM6 (Fig. 8c) and the cross-sectional area using the inflow thickness (5 ± 1 m, Fig. 6a and c) and the sill width (400 m). The deep-water volume (km^3) = the volume discharge rate × the renewal duration. The volume of the IAB deep layer is 0.12 km^3.

Deep-water renewal events in inner Ambon Bay (Dates/ Roman numerals)		Discharge of deep-water inflow (m^3/s)	Volume of deep-water (km^3)	% volume of the deep layer of IAB being flushed
The easterly monsoonal season	July 15, 2019 (I)	100 ± 20	0.017 ± 0.003	14 ± 3
	July 17, 2019 (III)	147 ± 29	0.013 ± 0.003	11 ± 3
	July 18, 2019 (IV)	108 ± 22	0.009 ± 0.002	8 ± 2
	July 19, 2019 (V)	195 ± 39	0.017 ± 0.003	14 ± 3
	July 20, 2019 (VII)	105 ± 21	0.003 ± 0.001	3 ± 1
	July 21, 2019 (VIII)	130 ± 26	0.009 ± 0.002	8 ± 2
	July 27, 2019 (XII)	176 ± 35	0.020 ± 0.004	17 ± 3
	July 28, 2019 (XIII)	76 ± 15	0.007 ± 0.001	6 ± 1
The transitional monsoonal season	October 5, 2019 (XVI)	83 ± 17	0.013 ± 0.003	11 ± 3
	October 7, 2019 (XVIII)	117 ± 23	0.018 ± 0.004	15 ± 3
	October 20, 2019 (XXII)	163 ± 33	0.015 ± 0.003	13 ± 3
	October 21, 2019 (XXIII)	192 ± 38	0.018 ± 0.004	15 ± 3
	October 22, 2019 (XXIV)	76 ± 30	0.013 ± 0.003	11 ± 3

internal surf at the slope causing tidal upwelling is likely to occur even with weak barotropic tidal flow (e.g. during the neap tide) if the sub-critical slope condition is met. In the easterly monsoonal season, sub-critical conditions predominate the OAB slope (S1–S5, Fig. 3c). When combined with extended periods of tidal flood in the neap phase, this creates favorable conditions for tidal upwelling, consistent with our observations (XII and XIII, Fig. 5a). Similarly, when combined with faster tidal currents associated with spring tides, tidal upwelling can occur (I – VIII, Fig. 5a). In contrast, the transitional monsoonal season is characterized by supercritical condition (Fig. 3c) in which the only mechanism for tidal upwelling is through rapid spring tide currents forcing deep-water to the sill, consistent with observations during spring tides (XIV – XXIV, Fig. 5b).

The magnitude of tidal upwelling in Ambon Bay (as measured by the depth from which water upwells) is controlled by the seasonally varying mechanisms for tidal upwelling. In the easterly monsoonal season, internal surf combines with flood tides to upwell water from depths as much as 200 m (Fig. 5g). In contrast, predominantly supercritical conditions during the transitional monsoonal season lead to downwelling that must be overcome by flooding tides to drive deep-water reaching the sill. As a result, tidal upwelling occurs from shallower depths (maximum of 115 m, Fig. 5g).

5.3. *Deep-water inflow along the sill of Ambon Bay*

Drivers of deep-water inflow at the sill are linked to the seasonal water stratification in OAB. In the transitional monsoonal season, deep-water inflow successfully crossing the sill predominantly relies on larger density difference between deep-water and the sill (Table 2), which is

more likely to be caused by strong stratified deep-water masses from OAB (Fig. 3b) arriving at the sill. This more-stratified upwelled water at the sill thus could drive the considerable baroclinic currents (Benjamin, 1968) transporting deep-water to the inshore sill. In contrast, in the easterly monsoonal season, deep-water arriving at the inshore sill is controlled by the tidal excursion of the deep-water inflow (Table 2) indicating the importance of advective tidal transport for deep-water inflow across the sill of Ambon Bay in this particular season. This is due to potentially weak baroclinic currents driven by insignificant deep-water/sill density difference (Benjamin, 1968) which is caused by less-stratified deep water from OAB (Fig. 3a) reaching the sill.

5.4. Deep-water renewal in inner Ambon Bay

In this study, we have improved the knowledge of flushing processes in the deep layer of IAB. With the assumption of steady-state inflow of deep-water of 0.01 m/s, Anderson and Sapulete (1982) estimated that the entire deep layer of IAB would be replenished in nine months. We have demonstrated that deep-water inflow occurs in pulses (Fig. 5a and b) not by steady-state processes and these pulses produce rapid deep-water inflow (0.05–0.1 m/s, Fig. 8c), causing approximately 80% and 40% volume of the IAB deep layer to be replenished within a spring-neap sequence in both easterly and transitional monsoonal seasons, respectively.

The seasonal IAB flushing is likely to determine the vulnerability of IAB to marine pollution. In the easterly monsoonal season, rapid flushing process in IAB is more likely to occur i.e. 80% volume of the IAB deep layer could be replenished by deep-water renewal pulses within a spring-neap sequence (i.e. ~2 weeks), similar to the renewal time of the entire IAB surface layer (14 days), caused by the freshwater flushing (Pello et al., 2014). This intense water renewal is considered to be important in preventing pollution build-up since high amounts of anthropogenic-derived pollutants are evident in the IAB linked to high rainfall rate in the easterly monsoonal season (Evans et al., 1995; Pelasula, 2008; Uneputty and Evans, 1997). Moderate water renewal in IAB is expected to occur in the transitional monsoonal season. This is due to low rainfall in this particular season (Tarigan, 1989) that can weaken the freshwater flushing at the IAB surface layer and the low frequency of deep-water renewal events in the IAB deep layer (Fig. 8b), causing only 40% volume of this layer to be replaced within a spring-neap sequence. This slow water renewal could drive greater pollution build-up in IAB.

5.5. Comparison with high-latitudinal fjords

While the intermittent nature of deep-water renewal during the spring-neap cycle is consistent for Ambon Bay and high-latitude shallow-silled fjords (Allen and Simpson, 1998; Geyer and Cannon, 1982)), a key difference is the velocity of deep-water inflow. The velocity of deep-water inflow in IAB ranges between 0.05 m/s and 0.1 m/s (Fig. 8c), much slower than that in high latitudinal fjords (0.1–0.4 m/s) (Allen and Simpson, 1998; Austin and Inall, 2002; Edwards et al., 1980; Gade and Edwards, 1980; Inall and Gillibrand, 2010; Liungman et al., 2001). Following the theoretical relationship between plume velocity and deep-water/sill density difference of Benjamin (1968, Equation 1.1), we predict that the difference in plume velocity observed in Ambon Bay compared with shallow-silled high latitude fjords will be due to the contrast in density difference between the locations. Using the above ranges of plume velocity, the relationship of density differences from theory is $\Delta\rho_{AB} = (0.18 \pm 0.12)\ \Delta\rho_{HL}$ (AB: Ambon Bay, HL: high latitude regions). This is confirmed by density differences based on observations: $\Delta\rho_{AB} = 1.02$ kg/m^3; $\Delta\rho_{HL} = 6.2 \pm 0.8$ kg/m^3 (Byfjorden, Sweden (Liungman et al., 2001),), $\Delta\rho_{HL} = 6 \pm 2$ kg/m^3 (the shallow sill at the seaward opening of Saguenay Fjord, Canada (Leduc et al., 2002; Seibert et al., 1979)). Note, high-latitude density difference values were calculated from observed salinity, applying the relationship developed by Stigebrandt (1981; $\rho = 1000 + 0.78(S)$) for areas in which temperature effects on density are negligible (such as the shallow sill of fjords).

Larger deep-water/sill density difference in shallow-silled fjords of high latitude regions than in Ambon Bay is likely due to the magnitude of freshwater inputs. Massive glacially-induced freshwater inputs in high-latitude regions (e.g. Milford Sound of New Zealand: 23 m^3/s, Doubtful Sound of New Zealand: 368 m^3/s, Loch Linnhe of Scotland: 80 m^3/s) (Allen and Simpson, 1998; Gade and Edwards, 1980; Pickard and Stanton, 1980; Stanton and Pickard, 1981) can produce considerably low water salinity at the sill fjord (e.g. typically $S = 20$–27‰) which thus causes larger deep-water/sill salinity difference from typical deep-water salinity, $S = 30.5$–34‰ (Leduc et al., 2002; Liungman et al., 2001; Seibert et al., 1979). In contrast, with similar deep-water salinity in Ambon Bay ($S = \sim$34‰, Fig. 6c), freshwater input in Ambon Bay (~14 m^3/s) (Pelasula, 2008; Putri et al., 2008; Siahaya, 2016) produces moderate low water density at the sill ($S = \sim$33.4‰) leading to small deep-water/sill density difference.

The latitudinal difference in water stratification appears to affect the degree of internal tidal dissipation in shallow-silled fjords between Ambon Bay and its high-latitude counterparts. Less thermal insolation in the high latitude region compared to the tropics (Fiedler, 2010; Sprintall and Cronin, 2009) leads to generally weaker water stratification in the high latitude region, on average, $N = 3.1 \times 10^{-3}$ s^{-1} (e.g. 3.3×10^{-3} s^{-1} in Knight Inlet of Canada, 4×10^{-3} s^{-1} in Dabob Bay of the US, 2.8×10^{-3} s^{-1} in Hood Canal of the US, 3.4×10^{-3} s^{-1} in Queens Reach of Canada, 3.2×10^{-3} s^{-1} in Princess Louisa Inlet of Canada, 1.8×10^{-3} s^{-1} in Kongsfjorden of Svalbard Archipelago in the Artic region) (Farmer and Smith, 1980; Inall et al., 2015; Smethie, 1980). These compare with values for OAB presented here of $N = 7$–12×10^{-3} s^{-1}. This difference has the potential to drive larger amplitude of internal tidal waves (hence, significant internal tidal dissipation) in the high latitudinal fjords than in Ambon Bay (Guo et al., 2016).

The difference in the length of fjord between fjords in the high latitude region and the tropics is likely to characterize oceanic water replenishing the fjord basin. In general, fjords in high latitudes are extremely long relative to their width due to their genesis by glacial pathways along fault lines extending from far inland (i.e. the head of fjord) to their seaward opening (e.g. Knight Inlet of Canada, ~60 km long; Oslofjord of Norway: ~50 km long, Puget Sound: ~160 km long) (Dowdeswell and Andrews, 1985; Nesje and Whillans, 1994). Thus, oceanic water from the seaward opening that reaches the fjord basin is more likely to have been profoundly modified during its journey. This is less likely to prevail in shallow-silled fjords in the tropical region which have short length to open ocean (e.g. Ambon Bay, 20 km; Darwin Bay of Galapagos, 2 km).

5.6. Lessons from observational techniques in this study

Internal tidal dissipation in the OAB slope in this study focused on its effects on deep-water renewal in IAB and did not consider offshore-directed overturning flows which may have potential hydrodynamic importance. Offshore-directed overturning flows can occur due to the horizontal density gradient between the water in the OAB slope and the offshore OAB driven by internal tidal-induced vertical mixing at the slope (Csanady, 1988; Joshi et al., 2017). Therefore, such outflow might have the potential to control the net circulation in OAB (Csanady, 1988; Joshi et al., 2017). To observe this convective overturning, the vertical density profile needs to be complemented by vertical profiles of ocean currents (Joshi et al., 2017). The use of 3D numerical models of circulation or moored ADCP instruments (Joshi et al., 2017) may be able to describe this overturning flow due to their three-dimensional nature.

The use of temperature loggers in estimating the speed of deep-water inflow in this study can be of interest to measurements of deep-water inflow in shallow-silled fjords. The comparable estimations of the speed of deep-water inflow between the temperature time lag method and the direct measurement using current meter CM6 in this study (Fig. 8c) give some confidence in the veracity of the use of temperature

loggers to measure this transport rate. Compared with the expense of a current meter unit, temperature loggers can offer a low-cost, robust oceanographic observation for studies of deep-water renewal in shallow-silled fjords.

Future studies related to deep-water inflow in the sill of Ambon Bay need to overcome logistical constraints of only daytime CTD measurements. Deploying temperature/conductivity loggers at multiple depths on moorings would enable continous monitoring of vertical profiles for these parameters leading to comprehensive observations of deep-water plumes in the sill.

6. Concluding remarks

In the shallow-silled tropical fjord of Ambon Bay, internal tidal upwelling events are more frequent during a spring-neap sequence in the easterly monsoonal season (13 events) due to the predominance of sub-critical slope condition than in the transitional monsoonal season (5 events). The magnitude of tidal upwelling in Ambon Bay as measured by the depth from which water upwells is stronger in the easterly monsoonal season (up to 200 m) than in the transitional monsoonal season (maximum: 115 m). Upwelled water successfully crossing the sill is controlled by the tidal excursion of the deep-water plume in the easterly monsoonal season and by the deep-water/sill density difference in the transitional monsoonal season. A series of deep-water renewal events in IAB within a spring-neap sequence (~2 weeks) in the easterly monsoonal season supplied a total inflow volume of 0.09 ± 0.02 km^3 which can replenish approximately 80% volume of the IAB deep layer. This total inflow volume was smaller in the transitional monsoonal season (0.05 ± 0.01 km^3), hence, only flushing 40% volume of the IAB deep layer.

High spatial and temporal resolution of oceanographic measurements in this study has allowed for a comprehensive understanding of internal tidal dynamics and deep-water inflow that affect the net circulation of Ambon Bay. Such comprehensive measurements had not been done in the past and thus, the existing numerical studies of ocean circulation in Ambon Bay did not account for these dynamics in their methodologies (Corvianawatie, 2014; Fadli and Radjawane, 2014; Noya et al., 2016, 2019; Putuhena, 2013). The new understandings of internal tidal waves and deep-water inflow in Ambon Bay presented here will be a key reference for future studies focused on water transport in Ambon Bay and other shallow-silled tropical fjords.

Credit author contribution statement

Gerry Giliant Salamena: as part of his PhD research, his roles were to conceptualize the research ideas, plan, design and conduct oceanographic observations in Ambon Bay of Indonesia, conduct data curation, Visualization and scientific analysis, and to write the original draft and revise it based on constructive feedback from co-authors. James C. Whinney and Scott F. Heron: as PhD supervisors, improving the initial research ideas on planning and designing oceanographic observations and on data analysis, reviewing and editing the original draft. Peter V. Ridd was involved with the early planning and design of this research and later improving ideas on oceanographic observations and on data analysis, reviewing and editing the original draft.

Declaration of competing interest

The authors declare no competing interest.

Acknowledgement

We would like to thank CTD operators (i.e. Willem M. Tatipatta, Sukisno, Wempi Barens, Idris, Rahman, Ferdy Kainama) and divers to deploy bottom current meters (i.e. Daniel Pelasula, Dominggus Polnaya, Jance Hehuat) from Centre for Deep Sea Research-LIPI (CDSR-LIPI) that supported our oceanographic campaign in Ambon Bay. We gratefully acknowledge Dr. Augy Syahailatua (former CDSR-LIPI director, 2009–2019) and Dr. Nugroho Dwi Hananto (current CDSR-LIPI director) who have been morally and administratively supportive for this campaign. We also thank research staff of Marine Geophysics Laboratory of James Cook University (MGL-JCU) (i.e. Simon, Brendan, Ben) for providing Marotte current meters (i.e. testing and calibration) for this oceanographic campaign. Financially, this study was made possible by the Australia Awards Scholarship of the Department of Foreign Affairs and Trade of Australian Government for PhD degree to Gerry Giliant Salamena and by MGL-JCU. Lastly, we thank two anonymous reviewers for their constructive comments to substantially improve our manuscript.

References

Alford, M.H., Klymak, J.M., Carter, G.S., 2014. Breaking internal lee waves at Kaena Ridge, Hawaii. Geophys. Res. Lett. 41, 906–912.
Allen, G.L., Simpson, J.H., 1998. Deep water inflows to upper Loch Linnhe. Estuarine. Coastal and Shelf Science 47 (4), 487–498.
Anderson, J.J., Sapulete, D., 1982. Deep water renewal in inner Ambon bay, Ambon, Indonesia. In: Gomez, E.D., Birkeland, C.E., Buddemeier, R.W., Johannes, R.E., Marsh Jr., J.A., Tsuda, R.T. (Eds.), The 4th International Coral Reef Symposium. Marine Science Center of University of Philippines, Manila, Phillippines, pp. 369–374.
Austin, W.E.N., Inall, M.E., 2002. Deep-water renewal in a Scottish fjord: temperature, salinity and oxygen isotopes. Polar Res. 21 (2), 251–257.
Baines, P.G., 1986. Internal tides, internal waves and near-inertial motions. In: Mooers, C.N.K. (Ed.), Baroclinic Processes on Continental Shelves Volume 3. The American Geophysical Union, Washington, pp. 19–31.
Belzile, M., Galbraith, P.S., Bourgault, D., 2016. Water renewals in the Saguenay fjord. J. Geophys. Res.: Oceans 121, 638–657.
Benjamin, T.B., 1968. Gravity currents and related phenomena. J. Fluid Mech. 31 (2), 209–248.
Berrangé, J.P., Thorpe, R.S., 1988. The geology, geochemistry and emplacement of the cretaceous—tertiary ophiolitic nicoya complex of the Osa Peninsula, southern Costa Rica. Tectonophysics 147, 193–220.
Bowden, K.F., 1983. Physical Oceanography of Coastal Waters. In: Ellis Horwood Series in Marine Science). Halsted Press, New York, p. 302.
Bruno, M., Vázquez, A., Gómez-Enri, J., Vargas, J.M., García Lafuente, J., Ruiz-Cañavate, A., Mariscal, L., Vidal, J., 2006. Observations of internal waves and associated mixing phenomena in the Portimao Canyon area. Deep Sea Res. Part II Top. Stud. Oceanogr. 53, 1219–1240.
Cacchione, D., Wunsch, C., 1974. Experimental study of internal waves over a slope. J. Fluid Mech. 66, 223–239.
Cacchione, D.A., Pratson, L.F., Ogston, A.S., 2002. The shaping of continental slopes by internal tides. Science 296 (5568), 724–727.
Corvianawatie, C., 2014. Mechanisms of Water Mass Circulation in the Ambon Bay Using Density Assimilation Model (In Indonesian Language). MSc. Thesis, Department of Oceanography of Institut Teknologi Bandung, Bandung, Indonesia.
Csanady, G.T., 1988. Ocean currents over the continental slope. In: Saltzman, B. (Ed.), Advances in Geophysics, ume 30. Elsevier, pp. 95–203.
Deuser, W.G., 1975. Reducing environment. In: Riley, J.P., Chester, R. (Eds.), Chemical Oceanography. Academic Press, London, pp. 1–37.
Dowdeswell, E.K., Andrews, J.T., 1985. The fiords of Baffin Island: description and classification. In: Andrews, J.T. (Ed.), Quaternary Environments: Eastern Canadian Arctic, Baffin Bay and West Greenland. Unwin, London, pp. 93–123.
Edwards, A., Edelsten, D.J., Saunders, M.A., Stanley, S.O., 1980. Renewal and entrainment in Loch Eil; a periodically ventilated Scottish fjord. In: Freeland, H.J., Farmer, D.M., Levings, C.D. (Eds.), Fjord Oceanography. Springer, Boston, MA, pp. 523–530.
Emery, K.O., Gunnerson, C.G., 1973. Internal swash and surf. Proc. Natl. Acad. Sci. U. S. A 70 (8), 2379–2380.
Evans, S.M., Dawson, M., Day, J., Frid, C.L.J., Gill, M.E., Pattisina, L.A., Porter, J., 1995. Domestic waste and TBT pollution in coastal areas of Ambon Island (Eastern Indonesia). Mar. Pollut. Bull. 30 (2), 109–115.
Fadli, M., Radjawane, I.M., 2014. Hydrodynamic Modelling in Ambon Bay (In Indonesian Language), Proceeding PIT X ISOI 2013. Indonesian Oceanologist Association, pp. 1–19.
Farmer, D.M., Freeland, H.J., 1983. The physical oceanography of fjords. Prog. Oceanogr. 12, 147–219.
Farmer, D.M., Smith, J.D., 1980. Tidal interaction of stratified flow with a sill in Knight inlet. Deep Sea Research Part A. Oceanographic Research Papers 27, 239–254.
Fiedler, P.C., 2010. Comparison of objective descriptions of the thermocline. Limnol Oceanogr. Methods 8, 313–325.
Friedrich, J., Janssen, F., Aleynik, D., Bange, H.W., Boltacheva, N., Çagatay, M.N., Dale, A.W., Etiope, G., Erdem, Z., Geraga, M., Gilli, A., Gomoiu, M.T., Hall, P.O.J., Hansson, D., He, Y., Holtappels, M., Kirf, M.K., Kononets, M., Konovalov, S., Lichtschlag, A., Livingstone, D.M., Marinaro, G., Mazlumyan, S., Naeher, S., North, R.P., Papatheodorou, G., Pfannkuche, O., Prien, R., Rehder, G., Schubert, C.J., Soltwedel, T., Sommer, S., Stahl, H., Stanev, E.V., Teaca, A., Tengberg, A.,

Waldmann, C., Wehrli, B., Wenzhöfer, F., 2014. Investigating hypoxia in aquatic environments: diverse approaches to addressing a complex phenomenon. Biogeosciences 11, 1215–1259.
Gade, H.D., Edwards, A., 1980. Deep water renewal in fjords. In: Freeland, H.J., Farmer, D.M., Levings, C.D. (Eds.), Fjord Oceanography. Springer, Boston, MA, pp. 453–489.
Geyer, W.R., Cannon, G.A., 1982. Sill processes related to deep water renewal in a fjord. J. Geophys. Res.: Oceans 87, 7985–7996.
Guo, D., Akylas, T.R., Zhan, P., Kartadikaria, A., Hoteit, I., 2016. On the generation and evolution of internal solitary waves in the southern Red Sea. J. Geophys. Res.: Oceans 121, 8566–8584.
Holtedahl, H., 1967. Notes on the formation of fjords and fjord-valleys. Geogr. Ann. Phys. Geogr. 49, 188–203.
Honthaas, C., Maury, R.C., Priadi, B., Bellon, H., Cotten, J., 1999. The Plio–Quaternary Ambon arc, eastern Indonesia. Tectonophysics 301, 261–281.
Houvenaghel, G.T., 1978. Oceanographic conditions in the Galapagos Archipelago and their relationships with life on the islands. In: Boje, R., Tomczak, M. (Eds.), Upwelling Ecosystems. Springer Berlin Heidelberg, pp. 181–200.
Inall, M.E., Gillibrand, P.A., 2010. The physics of mid-latitude fjords: a review. In: Howe, J.A., Austin, W.E.N., Forwick, M., Paetzel, M. (Eds.), Fjord Systems and Archieves, vol. 344. Geological Society Special Publications, London, pp. 17–33.
Inall, M.E., Nilsen, F., Cottier, F.R., Daae, R., 2015. Shelf/fjord exchange driven by coastal-trapped waves in the Arctic. J. Geophys. Res.: Oceans 120, 8283–8303.
Joshi, M., Rao, A.D., Mohanty, S., Pradhan, H.K., Murty, V.S., Prasad, K.V.S.R., 2017. Internal waves over the shelf in the western Bay of Bengal: a case study. Ocean Dynam. 67, 147–161.
Kakisina, T.J., Anggoro, S., Hartoko, A., Suripin, 2015. Analysis of the impact of land use on the degradation of coastal areas at Ambon Bay-Mollucas Province Indonesia. Procedia Environmental Sciences 23, 266–273.
Klymak, J.M., Alford, M.H., Pinkel, R., Lien, R.-C., Yang, Y.J., Tang, T.-Y., 2011. The breaking and scattering of the internal tide on a continental slope. J. Phys. Oceanogr. 41, 926–945.
Klymak, J.M., Buijsman, M., Legg, S., Pinkel, R., 2013. Parameterizing surface and internal tide scattering and breaking on supercritical topography: the one- and two-ridge cases. J. Phys. Oceanogr. 43, 1380–1397.
Klymak, J.M., Pinkel, R., Rainville, L., 2008. Direct breaking of the internal tide near topography: kaena Ridge, Hawaii. J. Phys. Oceanogr. 38, 380–399.
Kumar, N., Suanda, S.H., Colosi, J.A., Haas, K., Di Lorenzo, E., Miller, A.J., Edwards, C. A., 2019. Coastal semidiurnal internal tidal incoherence in the Santa Maria Basin, California: observations and model simulations. J. Geophys. Res.: Oceans 124, 5158–5179.
Leduc, J., Bilodeau, G., de Vernal, A., Mucci, A., 2002. Distribution of benthic foraminiferal populations in surface sediments of the Saguenay Fjord, before and after the 1996 flood. Palaeogeogr. Palaeoclimatol. Palaeoecol. 180, 207–223.
Legg, S., Klymak, J., 2008. Internal hydraulic jumps and overturning generated by tidal flow over a tall steep ridge. J. Phys. Oceanogr. 38, 1949–1964.
Leichter, J.J., Stewart, H.L., Miller, S.L., 2003. Episodic nutrient transport to Florida coral reefs. Limnol. Oceanogr. 48, 1394–1407.
Leichter, J.J., Deane, G.B., Stokes, M.D., 2005. Spatial and temporal variability of internal wave forcing on a coral reef. J. Phys. Oceanogr. 35, 1945–1962.
Lerczak, J.A., Winant, C.D., Hendershott, M.C., 2003. Observations of the semidiurnal internal tide on the southern California slope and shelf. J. Geophys. Res.: Oceans 108 (C3) (13-1)-(13-13).
Lewerissa, R., Sismanto, S., Setiawan, A., Pramumijoyo, S., 2018. The study of geological structures in Suli and Tulehu geothermal regions (Ambon, Indonesia) based on gravity gradient tensor data simulation and analytic signal. Geosciences 8, 1–21.
Liungman, O., Rydberg, L., Göransson, C.G., 2001. Modeling and observations of deep water renewal and entrainment in a Swedish sill fjord. J. Phys. Oceanogr. 31, 3401–3420.
Marchant, R., Stevens, T., Choukroun, S., Coombes, G., Santarossa, M., Whinney, J., Ridd, P., 2014. A buoyant tethered sphere for marine current estimation. IEEE J. Ocean. Eng. 39, 2–9.
Nahas, E.L., Pattiaratchi, C.B., Ivey, G.N., 2005. Processes controlling the position of frontal systems in Shark Bay, Western Australia. Estuar. Coast Shelf Sci. 65, 463–474.
Nesje, A., Whillans, I.M., 1994. Erosion of sognefjord, Norway. Geomorphology 9, 33–45.
Noya, Y.A., Kalay, D.E., Purba, M., Koropitan, A.F., Prartono, T., 2019. Modelling baroclinic circulation and particle tracking in Inner Ambon Bay. IOP Conf. Ser. Earth Environ. Sci. 339, 1–13.
Noya, Y.A., Purba, M., Koropitan, A.F., Prartono, T., 2016. Modeling the barotropic circulation on inner Ambon Bay. Int. J. Oceans Oceanogr. 10, 265–286.
Pearson, T.H., 1980. Macrobenthos of fjords. In: Freeland, H.J., Farmer, D.M., Levings, C. D. (Eds.), Fjord Oceanography. Springer, Boston, MA, pp. 569–602.
Pelasula, D., 2008. Impact of Deforestation on Upper Land to Marine Coastal Ecosystem on Ambon Bay (In Indonesian Language). MSc. Thesis, Faculty of Fishery and Marine Sciences. Universitas Pattimura, Ambon, Indonesia.
Pello, F.S., Adiwilaga, E.M., Huliselan, N.V., Damar, A., 2014. Effects of seasonal on nutrient load input the inner Ambon Bay (in Indonesian). Bumi Lestari J. Environ. 14, 63–73.
Petruncio, E.T., Rosenfeld, L.K., Paduan, J.D., 1998. Observations of the internal tide in monterey canyon. J. Phys. Oceanogr. 28, 1873–1903.
Pickard, G.L., Stanton, B.R., 1980. Pacific fjords - a review of their water characteristics. In: Freeland, H.J., Farmer, D.M., Levings, C.D. (Eds.), Fjord Oceanography. Springer, Boston, MA, pp. 1–51.
Pownall, J., Hall, R., Watkinson, I.M., 2013. Extreme extension across Seram and Ambon, eastern Indonesia: evidence for Banda slab rollback. Solid Earth 4, 277–314.
Putri, M.R., Mudjiono, Basit, A., 2008. Monitoring of Physical Oceanography in Ambon Bay (In Indonesian Language). Indonesian Institute of Sciences (LIPI), pp. 41–47. Proceeding PIT ISOI 2008.
Putuhena, H.S., 2013. Coupled 2D Hyrodynamic Model with Marine Debris Trajectory Model in Ambon Bay (Indonesian Language). BSc thesis, Department of Oceanography of Institute Teknologi Bandung. Bandung, Indonesia.
Rebert, J.P., Birowo, S., 1989. Internal wave in Ambon bay (in Indonesian language). In: Soemodigardjo, S., Birowo, S., Kasijan, R. (Eds.), Teluk Ambon II, Biologi, Perikanan, Oseanografi Dan Geologi. Balai Sumber Daya Laut, P3O LIPI, pp. 95–104. Ambon, Indonesia.
Saiya, H.G., Dibyosaputro, S., Santosa, S.H.B., 2016. USLE estimation for potential erosion at wae heru watershed and wae tonahitu watershed, Ambon Island, Indonesia. Indones. J. Geogr. 48, 191–205.
Sandstrom, H., Oakey, N.S., 1995. Dissipation in internal tides and solitary waves. J. Phys. Oceanogr. 25, 604–614.
Seibert, G., Trites, R., Reid, S., 1979. Deepwater exchange processes in the Saguenay fjord. Journal of the Fisheries Board of Canada 36, 42–53.
Siahaya, W.A., 2016. The Effects of Changes in Land Cover on the Changes in Coastal Benthic Cover of Small Island Based on the Analysis of Medium Resolution Satellite Image (The Case Study of 14 River Catchments Disharging into Ambon Bay) (In Indonesian Language). PhD Thesis, Department of Remote Sensing of Universitas Gadjah Mada, Yogyakarta, Indonesia.
Smethie, W.M., 1980. Estimation of vertical mixing rates in fjords using naturally occurring Radon-222 and salinity as tracers. In: Freeland, H.J., Farmer, D.M., Levings, C.D. (Eds.), Fjord Oceanography. Springer, Boston, MA, pp. 241–249.
Sobari, A., 2009. Analysis of the Economic Growth Rate in North Maluku Province 2000-2008 (In Indonesian Language). B.Ec Thesis, Faculty of Economy and Management. Bogor Agriculture Institute, Bogor, Indonesia.
Sprintall, J., Cronin, M.F., 2009. Upper ocean vertical structure. In: Steele, J.H. (Ed.), Encyclopedia of Ocean Sciences. Academic Press, pp. 217–224.
Staalstrøm, A., Aas, E., Liljebladh, B., 2012. Propagation and dissipation of internal tides in the Oslofjord. Ocean Sci. 8, 525–543.
Staalstrøm, A., Arneborg, L., Liljebladh, B., Broström, G., 2014. Observations of turbulence caused by a combination of tides and mean baroclinic flow over a fjord sill. J. Phys. Oceanogr. 45, 355–368.
Staalstrøm, A., Røed, L.P., 2016. Vertical mixing and internal wave energy fluxes in a sill fjord. J. Mar. Syst. 159, 15–32.
Stanton, B.R., Pickard, G.L., 1981. Physical Oceanography of the New Zealand Fiords. New Zealand Department of Scientific and Industrial Research, Wellington, New Zealand, p. 37pp.
Stigebrandt, A., 1976. Vertical diffusion driven by internal waves in a sill fjord. J. Phys. Oceanogr. 6, 486–495.
Stigebrandt, A., 1979. Observational evidence for vertical diffusion driven by internal waves of tidal origin in the Oslofjord. J. Phys. Oceanogr. 9, 435–441.
Stigebrandt, A., 1981. A mechanism governing the estuarine circulation in deep, strongly stratified fjords. Estuarine. Coastal and Shelf Science 13, 197–211.
Subeesh, M.P., Unnikrishnan, A.S., 2016. Observed internal tides and near-inertial waves on the continental shelf and slope off Jaigarh, central west coast of India. J. Mar. Syst. 157, 1–19.
Syvitski, J.P.M., Shaw, J., 1995. Sedimentology and geomorphology of fjords. In: Perillo, G.M.E. (Ed.), Development in Sedimentology. Elsevier, pp. 113–178.
Tarigan, M.S., 1989. Air and sea surface temperatures of the outer Ambon Bay (in Indonesian language). In: Soemodigardjo, S., Birowo, S., Kasijan, R. (Eds.), Teluk Ambon II, Biologi, Perikanan, Oseanografi Dan Geologi. Balai Sumber Daya Laut, P3O LIPI, pp. 121–131. Ambon, Indonesia.
Tarigan, M.S., Wenno, L.F., 1991. Upwelling in Ambon bay (in Indonesian language). In: Praseno, D.P. (Ed.), Perairan Maluku Dan Sekitarnya Volume. Balai Sumber Daya Laut, P3O LIPI, Ambon, Indonesia, pp. 141–146.
Uneputty, P., Evans, S.M., 1997. The impact of plastic debris on the biota of tidal flats in Ambon Bay (eastern Indonesia). Mar. Environ. Res. 44, 233–242.
van Oostenbrugge, J.A.E., 2003. Uncertainty in Daily Catch Rate in the Light Fisheries Around Ambon and the Lease Islands: Characterisation, Causes and Consequences. PhD Thesis. Wageningen University, Wageningen, The Netherdlands.
Wang, Y.-H., Dai, C.-F., Chen, Y.-Y., 2007. Physical and ecological processes of internal waves on an isolated reef ecosystem in the South China Sea. Geophys. Res. Lett. 34, 1–7. L18609.
Wenno, L.F., Anderson, J.J., 1984. Evidence for tidal upwelling across the sill of Ambon Bay. Mar. Res. Indones. 23, 13–20.